View metadata, citation and similar papers at core.ac.uk
brought to you by CORE
provided by Elsevier - Publisher Connector

Composite Structures 94 (2012) 1781–1792

Contents lists available at SciVerse ScienceDirect

Composite Structures

journal homepage: www.elsevier.com/locate/compstruct

Moderate speed impact damage to 2D-braided glass–carbon composites

M.P.F. Sutcliffe [a,*], C. Monroy Aceves [a], W.J. Stronge [a], R.S. Choudhry [b,1], A.E. Scott [c]

[a] Engineering Department, University of Cambridge, Trumpington Street, Cambridge CB2 1PZ, UK
[b] Northwest Composites Centre, University of Manchester, Sackville Street, Manchester M60 1QD, UK
[c] School of Engineering Science, University of Southampton, Southampton, Hampshire SO17 1BJ, UK

ARTICLE INFO

Article history:
Available online 5 January 2012

Keywords:
A. Hybrid
A. Fabrics/textiles
B. Impact behaviour

ABSTRACT

Hybrid glass–carbon 2D braided composites with varying carbon contents are impacted using a gas gun by impactors of masses 12.5 and 44.5 g, at impact energies up to 50 J. The damage area detected by ultrasound C-scan is found to increase roughly linearly with impact energy, and is larger for the lighter impactor at the same impact energy. The area of whitening of the glass tows on the distal side corresponds with the measured C-scan damage area. X-ray imaging shows more intense damage, at the same impact energy, for a higher-mass impactor. Braids with more glass content have a modest increase in density, decrease in modulus, and reduction in the C-scan area and dent depth at the impact site, particularly at the higher impact energies. Impact damage is found to reduce significantly the compressive strength, giving up to a 26% reduction at the maximum impact energy.

© 2012 Elsevier Ltd. Open access under CC BY license.

1. Introduction

Composite materials are widely used in applications requiring good specific stiffness and strength. However, there is a tendency for these materials to suffer more damage as a result of impact than equivalent metallic materials, either in the form of fracture of the relatively brittle fibres or due to cracking in the matrix [1]. Impact damage results in a reduction of the composite in-plane compressive strength. Braided textiles formed into composites using resin transfer moulding (RTM) are attractive for making high performance parts requiring impact tolerance. By including different weave patterns and tow materials the braid architecture can be tailored to give appropriate stiffness and impact resistance. Dry preforms can then be moulded in a reasonably cost-effective manner using RTM to give relatively complex components. Applications for braided materials can be found in various aerospace sectors including new-generation compressor casings for jet engines [2]. The aim of this paper is to determine the damage response of 2D-braided hybrid composite material at impact energies and speeds of concern in service use.

There are many forms of impact damage seen in composites, see for example the comprehensive reviews by Bibo and Hogg [3] and Abrate [4]. Damage occurs under the impactor in the form of matrix cracking and tow failure. Delamination due to matrix cracks between plies is seen through the thickness of the composite and damage associated with plate bending is observed on the distal side of the plate in the form of tensile fibre failure and tow splitting (i.e. matrix cracks along the fibre direction and typically transverse to the plane of the flattened tows). At high enough impact energies the plate perforates with extensive tow fibre failure. The exact nature of damage depends on the composite weave architecture, resin properties and the shape and speed of the colliding missile [1,5].

Woven materials have traditionally been used in impact-critical applications due to their superior ability, relative to unidirectional composites, to maintain structural integrity at significant impact energies [3]. Here the interlacing tow architecture can be used to limit damage, particularly delamination. Curtis and Bishop [6] show typical damage modes of delamination, crushing and compression buckling on the impact face, and fibre tensile failure on the distal face. Although there are many studies on the impact response of composites, including a range of woven composites, results for the impact resistance of braided composites are more sparse. Hosur et al. [7] give low-speed impact properties of carbon bi-axial and tri-axial braided plates of thickness around 2.3 mm. A drop tower was used to give impact energies up to 30 J. At the highest impact energy considerable damage was seen both on the impacted and distal faces, but the plates were not completely penetrated. The braided nature of the composite was found to help localise the damage.

Hybrid materials containing a mixture of fibres, for example glass and carbon, have been used to increase impact tolerance, taking advantage of the higher strain to failure of the glass fibres [8]. This is at the expense of increased density and reduced stiffness. A number of studies show a significant improvement in the impact response of carbon composites when glass is included;

* Corresponding author. Tel.: +44 1223 332996; fax: +44 1223 332662.
E-mail address: mpfs@eng.cam.ac.uk (M.P.F. Sutcliffe).
[1] Present address: National University of Sciences and Technology, College of E&ME Campus, Peshawar Road, Rawalpindi 46000, Pakistan.

0263-8223 © 2012 Elsevier Ltd. Open access under CC BY license.
doi:10.1016/j.compstruct.2011.12.026

this is true both for unidirectional [9] and woven [10–12] laminates. Hybrid braided material is straightforward to manufacture using tows of different materials and is an attractive option for impact-tolerant structures. There is very little information on the impact performance of this class of material, although results for a hybrid glass–carbon braid including 0° tows look promising [13].

Impact speed is an important factor in determining impact damage. Higher-speed impacts trigger different failure mechanisms because the deformation field induced by the impact includes higher frequency modes in addition to the fundamental (quasi-static) mode of deformation [14]. Ollson [15] details a theoretical model for the plate response. Instead of using impact velocity to characterise impact conditions, he shows that the ratio M/M_p of the projectile to plate mass determines the plate response. For $M/M_p < 0.23$ for a square plate, flexural waves do not reach the boundaries of the plate during the impact and the response is dominated by flexural waves. For $M/M_p > 2$ the response is quasi-static. For $0.2 < M/M_p < 2$ the impact is of an intermediate form with interaction between the dynamics and boundary conditions of the plate. This effect can be used to explain how, for the same impact energy, an increase in delamination was observed with a smaller impacting mass [15]. However, it should be noted that there are also contradictory results showing a reduced damage for smaller masses at the same impact energy, e.g. [16]. Perhaps the nature of the material and impact event created different types of damage in these different test setups. As has been noted in [3], the interaction between the dynamic structural response of the plate and the complex failure response of the composite makes it difficult to compare experimental results with different plate or impactor geometries or material architecture. There is also evidence that material properties change at high strain rates [8,17].

As noted above, the impact response of composites depends strongly on material, impact speed and geometry. Previous work by the authors [18] has presented preliminary results for a 2D braided glass–carbon composite. In this paper we undertake a more comprehensive examination of the impact response of this class of material, including the effect of the glass proportion and measuring the post-impact compressive strength. Impact energies up to 50 J were chosen so as to give significant damage to the plate, as these are the conditions of most interest in the post-impact performance of the structure. The damage incurred is assessed by a range of techniques. Although many tests are performed using drop-weight conditions with masses of several kilograms, impacts in service are likely to be at higher speeds with lighter masses. Hence, given the significance of dynamic effects, the tests reported here were performed using projectiles at speeds up to 83 m/s. To understand better the dynamic effects in the tests, the impactor speed and mass is varied and a careful image analysis algorithm is developed to extract the force–time history from videos of the impacting projectile.

2. Materials

Dry fabrics were braided using a 2×2 bias braid from tows of glass and carbon (1200 tex E-glass, 17 μm filament diameter) and 800 tex 12 k HTA 40 carbon (7 μm filament diameter). Three fabrics were woven, containing 50%, 75% or 100% of carbon tows. The weave pattern is illustrated in Fig. 1, showing in this case the 75% carbon braid in which every fourth tow in both weave directions is glass. For the 50% carbon braid alternate tows are glass. The nominal volume percentage of carbon in the dry fabrics was estimated from the nominal fibre density and tex and found to be very close to the tow percentage. This reflects the very similar volumes of the glass and carbon tows used.

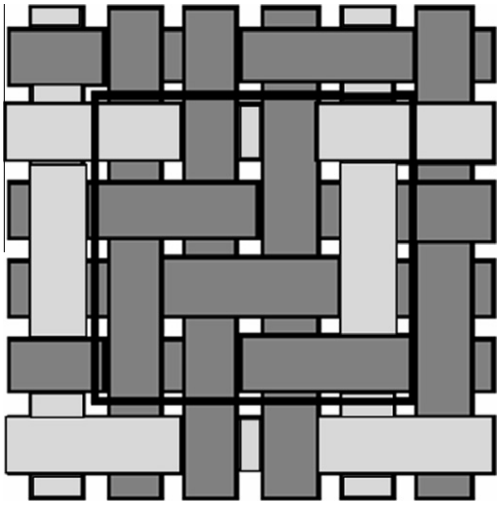

Fig. 1. Braid tow geometry for the 75% carbon material. The light shaded tows are glass.

Flat plates were resin transfer moulded from nine layers of the braided material with $a \pm 45°$ lay-up, using an epoxy resin (Huntsman Araldite LY 564 with Aradur 2954 hardener), to give a plate thickness of 4.34 ± 0.02 mm for all three materials. The tow width and thickness in the cured samples was around 3.3 mm and 0.25 mm, respectively. The panels were C-scanned (see details in Section 5) to identify and exclude any poor quality regions. No significant porosity was apparent in the C-scans or subsequent micrograph sections. Square samples with side length of approximately 130 mm were cut out for testing with the edges aligned with the bias direction (so that tows run along the plate diagonals). Plate thicknesses were measured from at least three samples, taking four measurements per sample. The fibre volume fraction was estimated from the pre-form areal density, the nominal dry-fabric density (to give the volume of dry fibre per unit area) and the final sample thickness. For all three materials the fibre volume fraction was estimated as 0.54. The constant volume fraction for the three materials reflects the way in which the glass and carbon tows have been matched in volume, also explaining why the panels had identical thickness. Samples were measured and weighed, and from this the mass density was deduced to be 1668, 1587 and 1461 kg/m^3 for the 50%, 75% and 100% carbon plates, respectively. The densities were very consistent, within 1.5% of the mean value for the three samples per panel measured.

3. Plate elastic property measurements

The elastic properties of the plate were measured for two reasons; firstly to provide reference properties for the material using a vibration measurement technique and secondly with a quasi-static test to provide input parameters for a quasi-static deformation analysis.

3.1. Vibration measurements

The 130×130 mm samples were suspended from two corners using cotton thread and then lightly tapped with an instrumented impact hammer. The response of the samples was measured using a light accelerometer attached to the plate and standard methods for experimental modal analysis were used to extract resonant frequencies and mode shapes.

Table 1
Undamaged sample resonant frequencies (Hz). Three sets of measurements are given for the 50% carbon braid.

% Carbon	Mode				
	1	2	3	4	5
50	723	904	1281	1977	2720
	712	902	1268	1972	2678
	701	878	1222	1916	2628
75	757	1023	1394	2188	3024
100	752	1153	1540	2391	3167

Table 2
Plate elastic properties. Three sets of measurements are given for the 50% carbon braid.

% Carbon	E_x (GPa)	G_{xy} (GPa)	v_{yx}	E_1 (GPa)	G_{12} (GPa)	v_{12}
50	14.9	17.4	0.66	38.8	4.50	0.11
	14.9	17.8	0.66	39.3	4.47	0.11
	15.7	18.5	0.65	40.4	4.78	0.094
75	15.7	21.4	0.68	46.2	4.66	0.078
100	14.3	24.9	0.75	53.2	4.07	0.068

Table 1 gives the resonant frequencies for the undamaged samples; measurements for three specimens with 50% carbon are included in the table. The first three resonances were used to extract plate stiffness parameters, using the methodology described by McIntyre and Woodhouse [19]. Table 2 gives the plate stiffness constants, with *xy* properties referred to the plate edges (along the bias direction) and 12 properties referred to the tow directions (i.e. at ~45° to the *xy* axes). Standard laminate stiffness rotation matrices are used to relate these properties. The stiffness values most influenced by tow stiffness (G_{xy} and E_1) increase as expected with the amount of carbon present. However the increase is not as great as might be expected given the significant difference between carbon and glass moduli because of the effect of crimp and matrix contributions.

To measure mode shapes the 50% carbon undamaged specimens were tapped on a 5 × 5 grid, centred on the centre of the specimen, with a nominal 25 mm spacing between grid points. *Q* factor results were taken from averaging these grid data (excluding outliers associated with loading on nodes). Mode shapes for the first three modes are given in Fig. 2, corresponding to cross (×), George cross (+) and ring (○) modes.

3.2. Static central-load tests

Static central-load tests were undertaken on 50% and 100% carbon samples, loading via a spherical indenter of radius 6.25 mm in the middle of the plate using a screw-driven universal testing machine at an indentation speed of 0.5 mm/min. The deflection was measured from the distal surface, so that local deformation distal at the contact was excluded. The plate was clamped using the same arrangement as for impact tests, as detailed in Section 4.1 and illustrated in Fig. 3. The plate stiffness $k = \delta/F$, where δ is the central displacement and F the applied force, was calculated from the slope of the force–displacement curve. Values for k were found to be 1.61 and 2.08 MN/m for the 50% and 100% carbon materials, respectively.

4. Test methodologies

4.1. Impact testing

Composite plates of size 130 × 130 mm were mounted on an aluminium support frame of thickness 12.5 mm using a steel clamp of thickness 10 mm. The clamp and support frame both had a square window of 100 × 100 mm and the clamp contained a slot to allow a side-on view of the impact site, as illustrated in Fig. 3. Calculations suggested that, while the frame was not rigidly fixed, it was sufficiently massive that movement of the support structure during the impact event was insignificant [20]. The samples were impacted by steel hemispherical-ended cylindrical impactors of tip radius 6.25 mm. Two impactors of mass either 12.5 or 44.5 g and corresponding lengths of 15 and 50 mm were used. The impactor was projected normal to the plate using a gas gun with a bore matching the diameter of the impactors, so that sabots were not needed. Energies up to 50 J were used, with corresponding peak velocities of 83 and 46 m/s for the light and heavy impactors, respectively. Videos showed that there was little rotation of the impactor between leaving the gas gun exit and hitting the sample (maximum angles of 5° and 10° for the large and small impactors, respectively), and that the rebound was close to normal (less than a 10° deviation) with small rotation velocities. The maximum error in the rebound energy associated with the component of the velocity not normal to the plate and with the angular velocity of the rebounding impactor was estimated from the videos as being 0.1 J.

High speed photography using a Phantom v640 camera was used to determine the impact and rebound speeds and infer the contact force from the projectile acceleration. A frame rate of 39,000 frames per second and an exposure time of 4.3 μs was used, with a spatial resolution in the image of 0.27 mm/pixel. The location of the trailing edge of the impactor was used to track the position of the impactor as a function of time. Sub-pixel resolution for identifying this edge was attained by fitting a quadratic function to the image intensity gradient. Velocity and acceleration were taken by numerically differentiating the position with respect to time. The contact force was taken as the mass of the impactor multiplied by its deceleration. It is assumed that the contact time is sufficient to allow stress waves to propagate through the impactor and for it to reach equilibrium. Fig. 4 shows typical analysis of

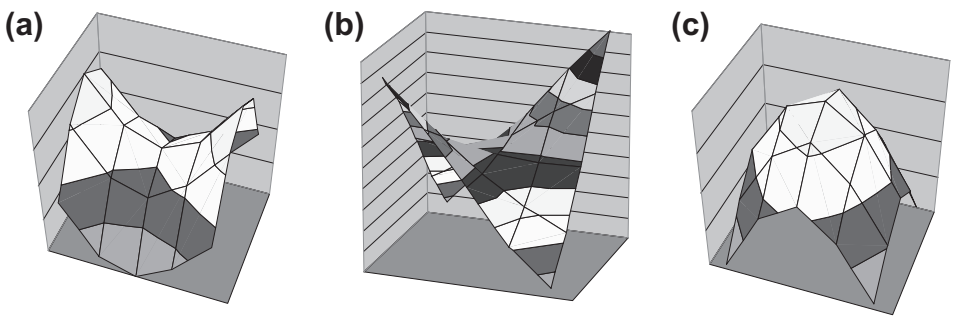

Fig. 2. Mode shapes; (a) mode 1 – cross (690 Hz), (b) mode 2 – George cross (856 Hz), and (c) mode 3 – ring (1206 Hz).

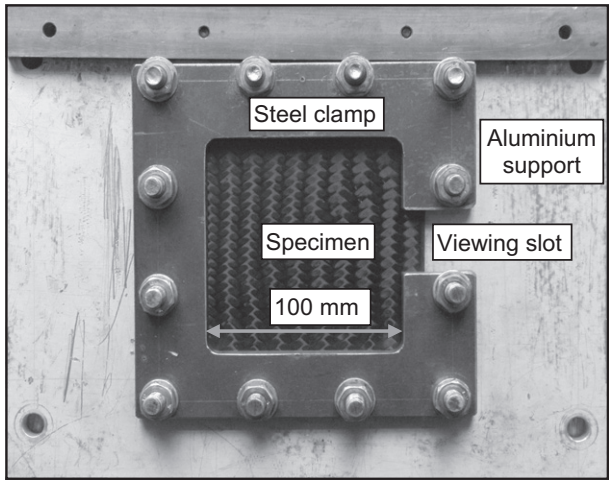

Fig. 3. Photograph of plate clamping arrangement. The aluminium support has a 100 × 100 mm window matching that of the steel clamp.

the image data. Since the process of inferring acceleration and hence force requires numerical differentiation twice, the process is susceptible to errors associated with noise in the data. The scatter in the inferred acceleration before and after contact, when the deceleration is expected to be effectively zero, gives an indication of the error inherent in this measurement. With typical maximum values of acceleration in these free-flight phases of around 0.015×10^6 m^2/s, force estimates for the light and heavy impactor may be in error by up to 0.2 and 0.7 kN respectively. With peak contact forces in the range 5–10 kN, these errors are acceptable. Further analysis of the accuracy of the force history is given in Appendix A.

4.2. Static indentation test

Quasi-static indentation tests were undertaken on each of the three materials to allow comparison with the dynamic impact results. A plate with the same dimensions as for the impact tests was supported on its back face by a washer of internal diameter 16 mm sitting on a rigid flat platen. The top face was loaded above the centre of the washer by a spherical indenter of radius 6.25 mm, using a screw-driven universal testing machine at an indentation speed of 0.5 mm/min. This washer-support arrangement was adopted to provide a localised deformation at the indent site more appropriate to the higher speed tests, where inertia of the plate inhibits bending of the whole plate.

4.3. Compression after impact (CAI) testing

The 130 × 130 mm samples containing 50:50 glass:carbon were tested in compression after being impacted. A purpose-built jig was constructed to support the edges of the panels and prevent macro-buckling, akin to the standard Boeing CAI test geometry (Boeing BSS 7260). Opposite faces were ground flat and parallel, to give specimen in-plane dimensions within a few millimetres of the original values of 130 × 130 mm. The samples were loaded across these faces, i.e. along the bias direction, in an Instron testing machine at a loading rate of 1 mm/min, with the load introduced using flat platens. The nominal stress was found from the specimen width and thickness of 4.34 mm. The end compression of the specimens was calculated from the cross-head displacement and used to give a nominal strain, dividing by the length of the specimen. A relatively small correction was made for the machine compliance, measured using a massive steel block in place of the specimen. The maximum damage area recorded in the impact samples of 2460 mm^2 corresponds to a diameter of 56 mm, equal to 43% of the specimen width in these tests.

5. Damage assessment methods

There are a variety of methods, both destructive and non-destructive, available to assess the damage incurred during impact of composites. As well as traditional techniques, recent innovations have included shearography [21], non-linear acoustic/ultrasound methods [22] and X-ray/synchrotron examination [23]. In this paper we focus on established methods that can provide either qualitative information about the damage mechanisms or robust

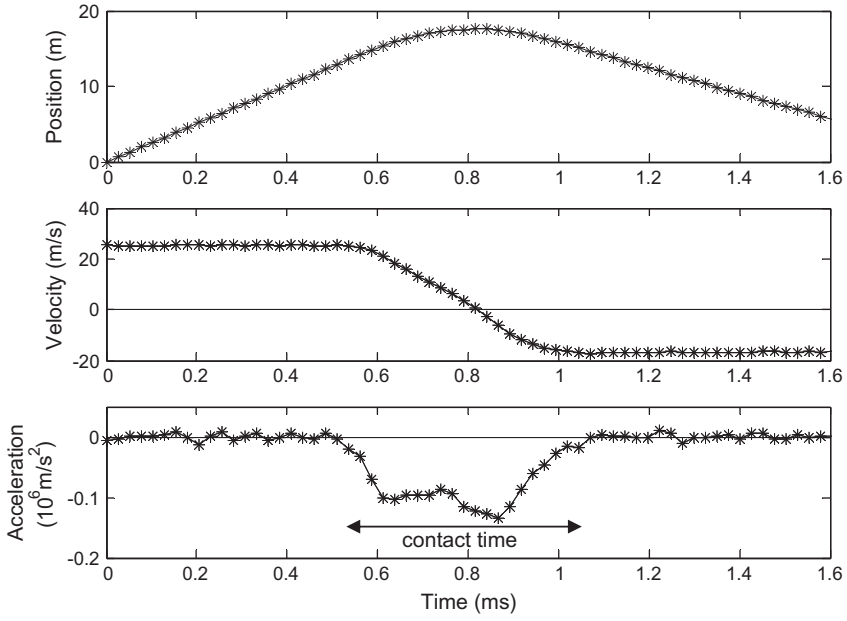

Fig. 4. Position, velocity and acceleration of rebounding impactor deduced from high speed camera images. Impact velocity = 25.3 m/s, impact energy = 14.3 J, 75% carbon braid, 44.5 g impactor. The contact time is estimated directly from the video.

quantitative data to characterise the damage. These techniques provide complementary information about the damage observed.

Ultrasonic C-scanning was undertaken using a MIDAS NDT water-jet inspection system, using an unfocussed 5 MHz probe in transmission mode and a 50 mm/s scan rate. The damage area was found by applying a suitable intensity threshold.

Contact profilometry was performed using a Taylor Hobson Form Talysurf 120 to measure the maximum crater depth at the impact site and the permanent indent in the quasi-static indentation tests. Although the instrument is able to resolve sub-micron features, potential errors arise from missing the lowest part of the crater and in identifying the nominal reference plane away from the crater. These errors were minimised by using multiple traverses to identify the deepest part, and by traversing the plate over a length significantly longer than the damaged region so that the surrounding undamaged material was included in the trace. The resulting error in these measurements is estimated as being less than 10 μm. Samples were stored in standard laboratory conditions between tests, with occasional substantial gaps of time between various testing phases. While the possibility of relaxation due to moisture uptake in the dents cannot be excluded, the dents were sufficiently deep that such effects would probably be minor.

The visual appearance of the specimens on their impact and distal faces was recorded using a standard flat bed optical scanner at a resolution of 300 dpi.

Sections of selected specimens were obtained by slicing specimens through the damage area using a Struers Accutom-50. The samples were polished, and imaged using a BX51 Olympus microscope.

Micro-CT X-ray imaging was undertaken using a 225 kV Nikon/Metris HMX. Two 75% carbon samples of 4.5 × 4.5 mm^2 cross-sections and approximately 47 mm and 34 mm in length were measured. These samples had been impacted at the same nominal energy of 35 J but with the different masses. The specimens were scanned in three sections along the length of the samples, with a resolution of 9.9 μm and 6.2 μm. A beam energy of 70 kV and current of 90 μA was used with a two second exposure. Two-dimensional radiographs were recorded at 2544 angular positions over 360° of rotation via a 2 × 2 k flat panel detector. Before imaging, the samples were placed in a zinc iodide bath for 5 min to facilitate the detection of microcracks within the composite.

Vibration measurements of frequency and Q factor, similar to those for elastic properties as described in Section 3.1, were made on the 50% carbon material. Tests were undertaken on both undamaged samples and samples impacted by both light and heavy projectiles to explore the effect of damage on the vibration response. None of the plate measurements were 'before-and-after' comparisons, making results prone to differences in plates, e.g. tow orientation differences.

6. Damage assessment results

6.1. C-scan

C-scan data differentiated clearly between the undamaged regions of the plate and a roughly circular damaged region around the impact site (Fig. 9 shows typical scans). Fig. 5 plots the damage area as a function of impact energy for the three plate materials and two impactor masses. The damage area increases roughly linearly with the impact energy for a given material and impactor mass. However there are significant differences between sets of data, with the damage area being significantly smaller for the heavier impactor at the same energy. The 50% carbon material shows the smallest damage area, with the 75% and 100% carbon braids having roughly similar damage. Only one sample was perforated,

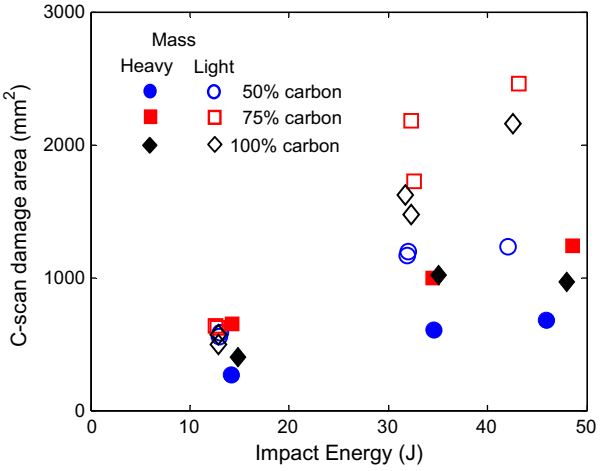

Fig. 5. Effect of impact energy on measured damage area using C-scanning.

the 100% carbon braid with the highest impact energy of around 50 J, impacted by the heavier projectile.

6.2. Profilometry

Fig. 6 plots the dent depth, measured by contact profilometry, as a function of impact energy. The dent depth increases roughly linearly with impactor energy. For the light impactor there is no apparent difference between materials, while for the heavy impactor the 100% carbon material has significantly larger dents than the other materials at the same energy. Two heavy-impactor samples (35 J, 100% carbon and 49 J, 75% carbon samples) suffered severe denting with significant tow damage visible on the distal surface, while the 100% carbon plate was perforated by the heavy impactor striking at an impact energy of 48 J. At the highest energy of around 45 J with a heavy impactor, the 50% carbon plate did not suffer from the extensive damage that was seen in corresponding plates with lower percentages of glass.

6.3. Observations: visual images, sectioning and X-ray imaging

Fig. 7 presents sections of damaged samples impacted at an energy between 32 and 35 J. The X-ray images, Fig. 7a–d are for 75% carbon braid. The zinc iodide is effective at highlighting cracks in

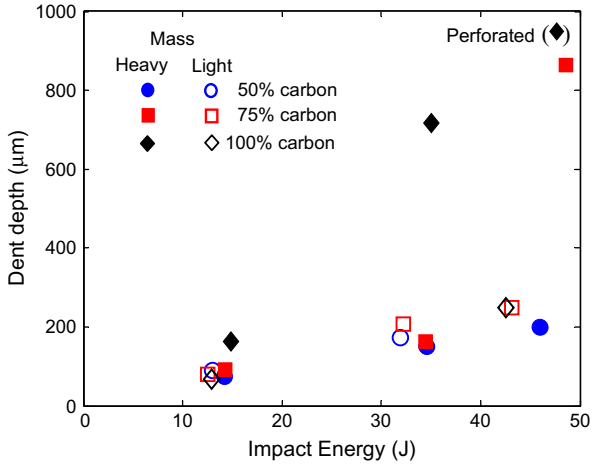

Fig. 6. Effect of impact energy on measured dent depth using profilometry.

the X-ray images, while the glass tows are also seen as bright regions. For the lower mass impactor, Fig. 7a and the corresponding enlargement in Fig. 7c, damage near the indenter site is observed in the form of matrix cracks leading to tow splitting and delamination. For the higher mass impactor, Fig. 7b and the corresponding enlargement in Fig. 7d, much more intense damage is observed directly under the impactor extending through to the distal face. Some tow fibre fracture is seen, but also extensive matrix cracking leading to tow splitting and delamination. In both cases the tow splits form a typical 'pine tree' cone of damage originating from the impact site [3]. Optical sections confirmed this picture, though it was more difficult to make out delaminations in these images. Fig. 7e shows an optical image for 100% carbon braid impacted by the heavier projectile at an energy of 35 J. The figure shows significant tow fibre fracture near the impact site. This sample was one of the two samples with a substantial permanent dent. Damage areas as detected by C-scanning were 2180 and 998 mm^2 for the X-rayed samples which had been impacted by the low and high mass impactors respectively, to give corresponding effective C-scan damage diameters of 53 and 36 mm. The location of the edge of the C-scan area has been included on the X-ray images, Fig. 7a and b, being near the edge of the sample in both cases.

Fig. 8 presents 3D images in which the carbon and glass has been digitally removed to reveal the cracks identified by zinc iodide in the two samples. These results show that cracking is prevalent throughout the sample impacted by the heavy mass, Figs. 7b and 8d, but does not extend to the right-hand end of the specimen that was impacted by the lighter mass, Figs. 7a and 8b. Since the edge of the C-scan damage area is near the right-hand end of the sample in both cases, this indicates that the C-scan damage area does not correspond to the relatively wide cracks which can be seen in these images. Presumably the periphery of the C-scan damage area is associated with microcracks either too small to be resolved by the X-ray imaging, or perhaps too small or not connected with the exterior to allow take-up of zinc iodide.

Fig. 9 compares the C-scan results and the flat-bed scanner visual images of the distal surface of 50% carbon braids, with the two impactor masses at an impact energy of 50 J. Significant matrix damage, probably in the form of matrix debonding, is clearly seen in the glass tows as a significant whitening. Corresponding damage is presumably present but not visible in the carbon tows. This whitening appears to be more intense for the heavier impactor, at comparable impact energies, but not as widespread as for the lighter impactor. The area detected as damage by C-scanning (approximated by the circles superimposed on the figures), corresponds to the observed areas of whitening, suggesting that this

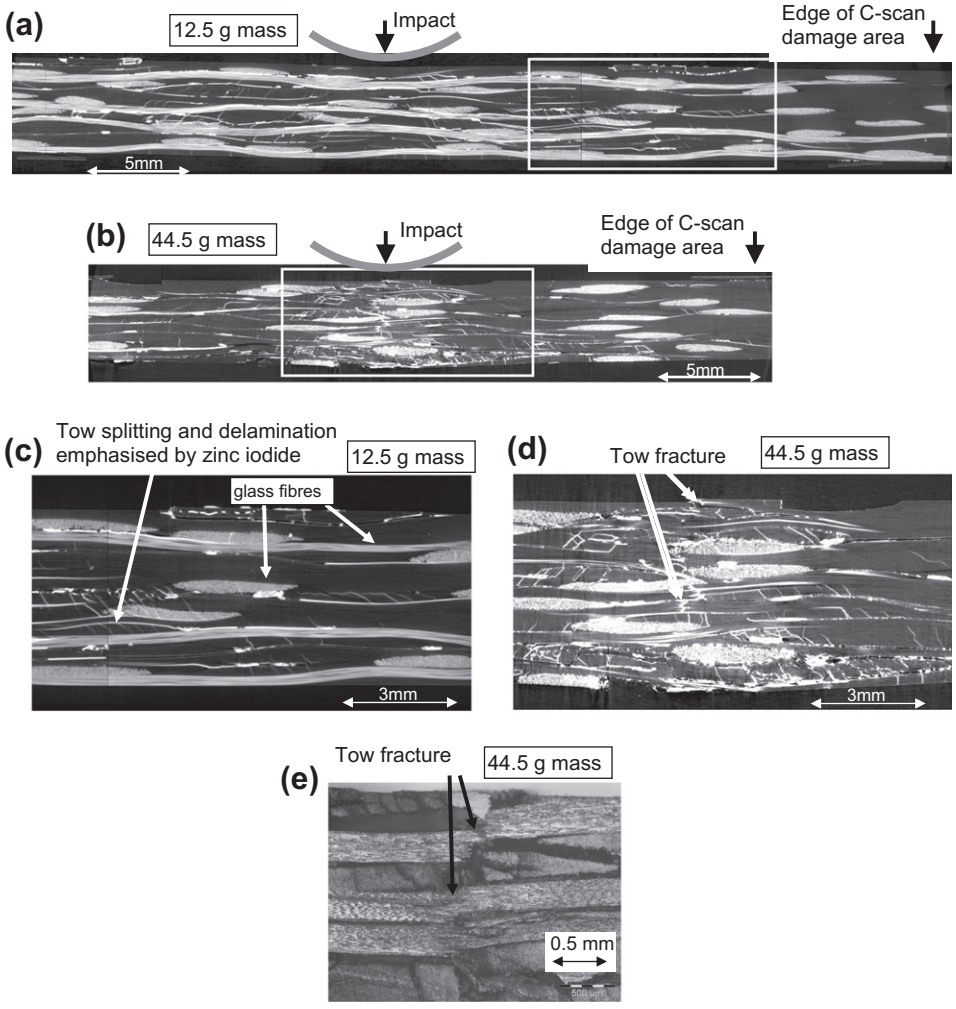

Fig. 7. X-ray images and optical micrograph near the impact site. All specimens have an impact energy between 32 and 35 J. (a) and (c) X-ray images, 75% carbon material, 12.5 g impactor, box on (a) indicates region covered by (c), (b) and (d) X-ray images, 75% carbon material, 44.5 g impactor, box on (b) indicates region covered by (d), and (e) optical micrograph, 100% carbon material, 44.5 g impactor.

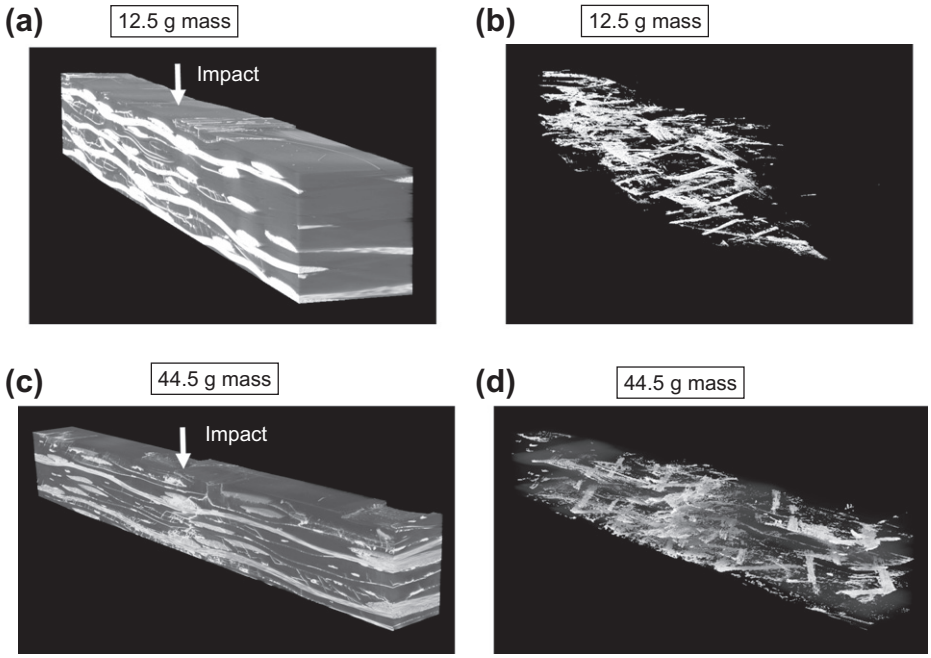

Fig. 8. X-ray analysis of samples seen in Fig. 7 with 75% carbon material; on left images of whole X-ray specimen, on right glass and carbon made transparent to reveal delamination and tow cracks: (a) and (b) 12.5 g impactor, sample size 4.5 × 4.5 × 47 mm and (c) and (d) 44.5 g impactor, sample size 4.5 × 4.5 × 34 mm (note that these images cover a significantly smaller section than that of images (a) and (b)).

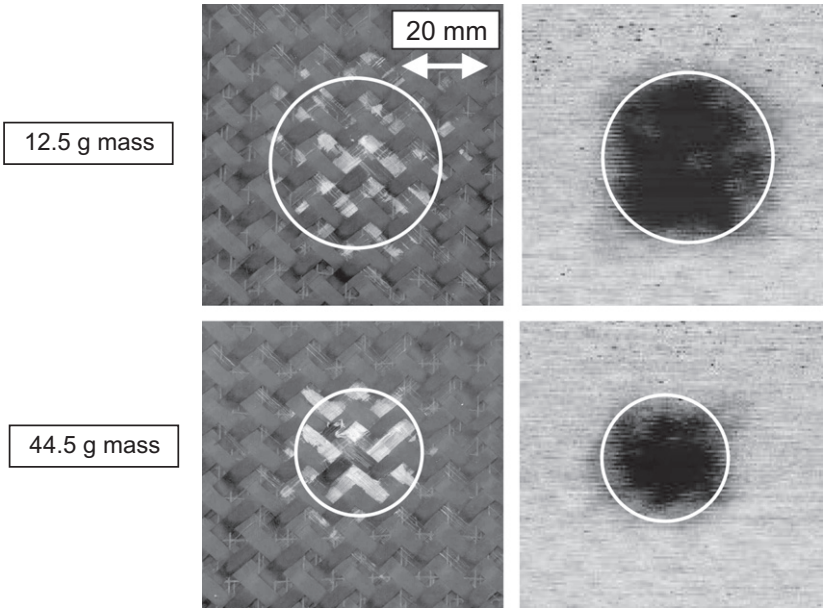

Fig. 9. Comparison of optical views of the distal face and C-scan images, 50% carbon material, nominal impact energy = 50 J: left – optical, right – C-scan, upper – 12.5 g impactor, lower – 44.5 g impactor. All images are to the same scale. The circles superimposed on the images have an area equal to that derived from the C-scan thresholding procedure (1235 mm^2 and 680 mm^2 for the 12.5 and 44.5 g masses, respectively).

matrix damage is the predominant form of damage detected by the C-scan data. This would also explain the poor correlation between tow-splitting and delamination damage, as indicated by X-ray imaging and sectioning, and the C-scan area seen in the samples.

6.4. Vibration measurements

Although we would expect a drop in resonant frequency with increasing impact energy associated with a drop in plate stiffness, this was not observed. Instead results for the first three modes were characterised by random variations of up to 3% between measurements, perhaps associated with geometric and material differences between samples. Apparently the damage did not make a significant change to the response for these whole-plate modes, even though up to 15% of the area of the plate in these samples was identified as being damaged by C-scanning. Probably 'before and after' measurements would be needed to give the accuracy required for such a study. However a consistent drop in Q factor (and so increased damping) with increasing impact energy was observed for the ring mode of vibration with the 50% carbon braid,

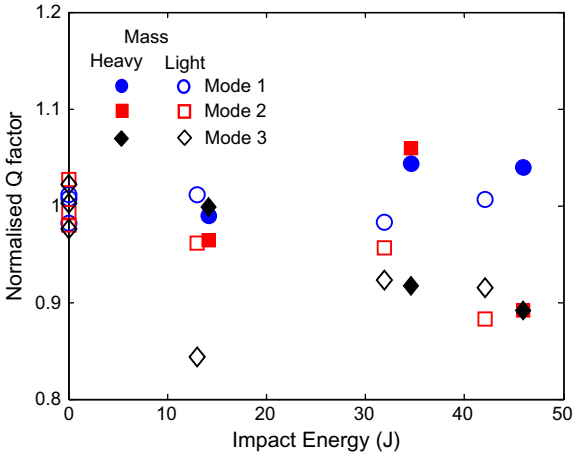

Fig. 10. Effect of impact damage on modal Q factors, normalised by the mean value for undamaged samples (50% carbon braid).

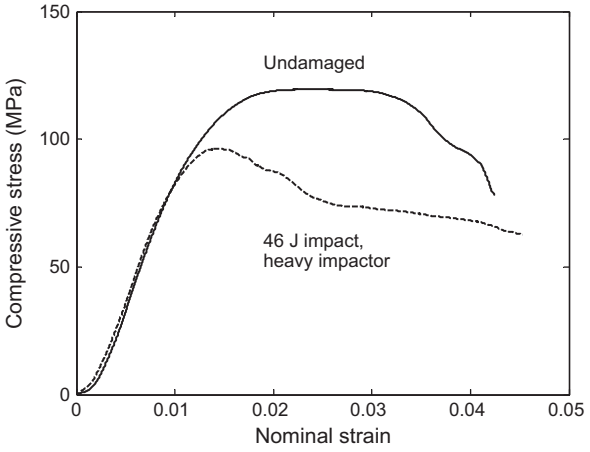

Fig. 11. Typical compression-after-impact failure response.

see Fig. 10. The Q factors have been normalised in this figure by a mean Q factor for the undamaged samples (with values of 62, 287 and 131 for modes 1, 2 and 3, respectively). It is interesting to note that mode 3, which has an anti-node at the impact site, is the one associated with the drop in Q factor. One data point at an impact energy of 13 J appears to be anomalous, probably reflecting difficulties with measuring the Q factor accurately.

6.5. Summary of damage detection results

A range of damage detection methods have been used to identify the effect of material, impact speed and energy on damage. Increasing glass content gives a consistent reduction in C-scan damage area for both impactor masses, and a reduction in permanent dent depth at the higher impact energies for the heavy impactor. For samples where glass tows were present, visual inspection of the surface reveals a similar extent of damage (presumably due to matrix debonding) as seen by C-scanning. The internal damage is clearly visualised by micro-CT X-ray imaging. Considerable matrix cracking leading to tow splitting and delamination is observed, along with some tow fibre fracture. This damage is more intense for the high-mass impactor, at the same energy. The extent of the matrix cracking detected by X-ray imaging does not correlate with the C-scan damage area. Apparently some more minor cracks or debonds detected as damage using the C-scan data were not detectable with the X-ray imaging. In effect impact with the heavier projectile, although giving a smaller C-scan damage area, is characterised by more severe damage under the impact site. This picture of more severe damage with the heavy impactor is consistent with some of the dent measurements, see Fig. 6, which show a significantly deeper dent with the heavier impactor at the same energy for all the 100% carbon specimens and for the high-energy 75% carbon case. Vibration measurements showed a drop in Q factor with increased impact energy. Although this method does not quantify the damage area, nevertheless it is a simple non-destructive tool which can provide useful data.

7. Compression after impact results

Compression after impact (CAI) tests have been used to measure the effect of impact damage on residual strength of plate specimens loaded by edge compression. Fig. 11 shows a typical response. Failure of the plates was progressive, but with a marked maximum in the load. Failure occurred at the impact site of the damaged samples, with some bulging observed and considerable shear both at the impact site and running outwards along the tows. Similar failure mechanisms were observed in the undamaged specimens, but with damage originating at random locations on the sample.

Fig. 12 plots the maximum CAI stress as a function of impact energy (note the discontinuity in the *y*-axis scale). Because the material is loaded in the bias direction the failure stresses are relatively low. There is a significant fall in compressive strength of up to 26% with increasing impact energy, with a similar behaviour for the small and large impactor masses. Specimens with no impact damage could in theory have suffered from some stress concentration effects at the loading points. However the relatively damage-tolerant behaviour for loading along the bias direction (c.f. Fig. 11) suggests that such effects would be slight. Curtis and Bishop found no effect of damage due to a 7 J impact on CAI strength of woven angle plies loaded as here along the bias direction [6]. In their case the area of damage was around 350 mm^2, comparable with that seen for the 13 J impact tests in this study and consistent with the very slight reduction in strength for these 13 J impacts, see Fig. 12.

Although the details of the damage area and damage intensity were different for the two impactor masses at equal energies, the compression-after-impact response is similar. Apparently the less severe and more distributed damage for the lighter impactor is equivalent to the more localised and severe damage for the heavier impactor in these cases.

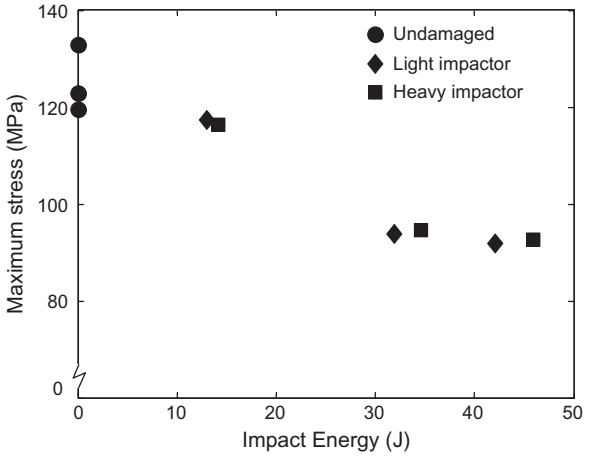

Fig. 12. Compression after impact strength, 50% carbon panels.

8. Impact mechanics

In this section further results relating to the impact mechanics are described, with the aim of helping understand the nature of the impact event and mechanisms causing damage.

The videos were used to identify the time of compression, from first contact to maximum plate deflection. This was around 130 and 260 μs for the light and heavy impactors, respectively, independent of the material. There was only a relatively modest increase of contact time with impact energy (changing by around 30% over the range of impact energies considered).

Fig. 13 plots the rebound energy as a function of impact energy. In the main the curves follow two straight lines, as included in the figure, with more energy retained by the high-mass than the low-mass projectile. The lines fitted through the heavy and light projectile data correspond to the rebound energy equalling 40% and 22% of the impact energy, respectively. Three data points identified in the figure that are off these linear fits, correspond to cases where severe dents and fibre damage were observed. The linearity between impact energy and rebound energy for all but a few tests suggests that an elastic model of the impact may be appropriate. Some of the energy lost from the impactor goes into inelastic deformation of the plate at the contact, but much of the energy is transferred to plate kinetic energy.

Fig. 14 plots the variation of inferred maximum contact force with impact energy for the different tests. The peak contact force is roughly independent of material and projectile mass, increasing with impact energy. The three samples with severe damage on the impact face have a contact force below the trend for the other samples. A first approximation to the plate response can be made by assuming quasi-static linear-elastic behaviour, with a plate stiffness k relating the contact force F and the central plate deflection δ. Equating the impact kinetic energy T_I with the stored elastic energy in the plate at maximum deflection gives a relationship for the maximum contact F_m as

$$F_m = \sqrt{2kT_I} \tag{1}$$

The measured plate stiffnesses taken from the centrally-loaded static tests (Section 3.2) with 50% and 100% carbon are used to plot theoretical curves in Fig. 14. The relatively slight change in modulus and stiffness between the different materials results in only a small change in the predicted contact force. The quasi-static analysis provides a fair first-approximation to the measured maximum contact force. However the peak force falls significantly below the

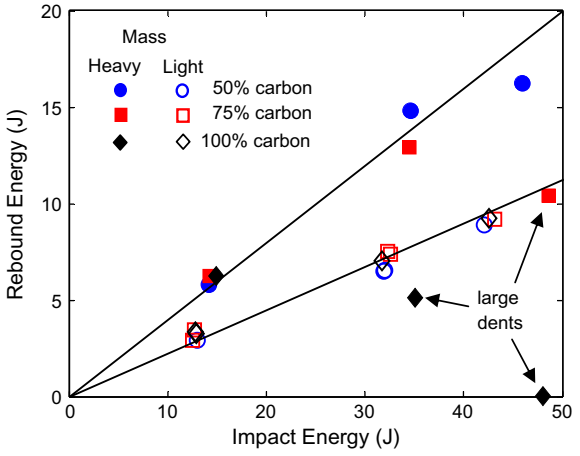

Fig. 13. Variation of rebound energy with impact energy. Trend lines added to the figure exclude the three data points with large dents.

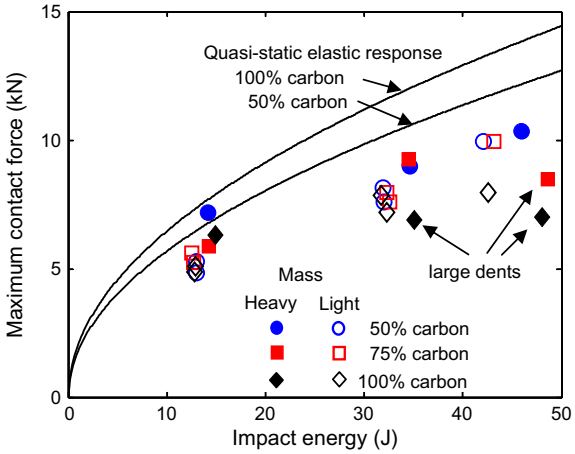

Fig. 14. Effect of impact energy on peak contact force.

elastic predictions at higher impact energies, demonstrating that a more sophisticated dynamic model is required to capture the details of the impact event.

Further details of the nature of the contact event are revealed by the variation of contact force with time, plotted in Fig. 15 for selected impacts typical of all the cases measured. Recall that errors in the inferred force are estimated as being 0.2 and 0.7 kN, for the small and large impactors respectively, so that random deviations of this order should be ignored. Results for the lighter impactor shown in Fig. 15a show a relatively short load pulse and a second small peak. The form of the curve is similar for the two materials and two impact energies. The small third peak apparent in one case is likely to be due to errors in tracking the impactor after it leaves the specimen. For the heavier impactor, Fig. 15b, three of the tests show a similar shape for the 50% and 100% carbon braids, with higher loads at the higher impact energy. The different form of curve seen for 100% carbon material at an impact energy of 48 J is because this was the specimen that was perforated.

To understand better the results, it is useful to apply Ollson's approach for characterising the plate response. Using the 75% carbon plate as typical and taking a plate mass corresponding to the unsupported area of 100 × 100 mm, the ratio M/M_p of the impactor to plate masses equals 0.18 and 0.65 for the 12.5 or 44.5 g projectiles, respectively. Hence, using Ollson's criterion for low-mass impacts of $M/M_p < 0.23$, we expect a significant difference between these sets of results. The response should be dominated by flexural waves for the smaller impactor, but for the larger impactor the response should be closer to the quasi-static mode. The double peaks in the contact force seen in Fig. 15 confirm that the dynamic response of the plate is important. As with the results of Ollson, who observed larger delamination areas for lower-mass impactors, this transition from quasi-static to flexural bending modes can explain the observed difference between the different projectile masses in the amount of damage identified by C-scanning. At equivalent impact energies, the higher-velocity, lower-mass impactor gives more localised deformation under the impactor. As the flexural wave travels from the impact site it is hypothesised that a wider area sees the corresponding higher curvatures and strains on the distal face. This would lead to the larger observed C-scan damage area for the lighter indenter at the same impact energy as seen in Fig. 5.

Fig. 16 shows that there is a reasonable correlation of dent depth with maximum force, although the plates impacted by the heavy projectile appear to have smaller dents than those impacted by the light projectile at the same peak force. The three specimens with very significant damage (including perforation) fall outside this band of results. Also included on the figure are the permanent

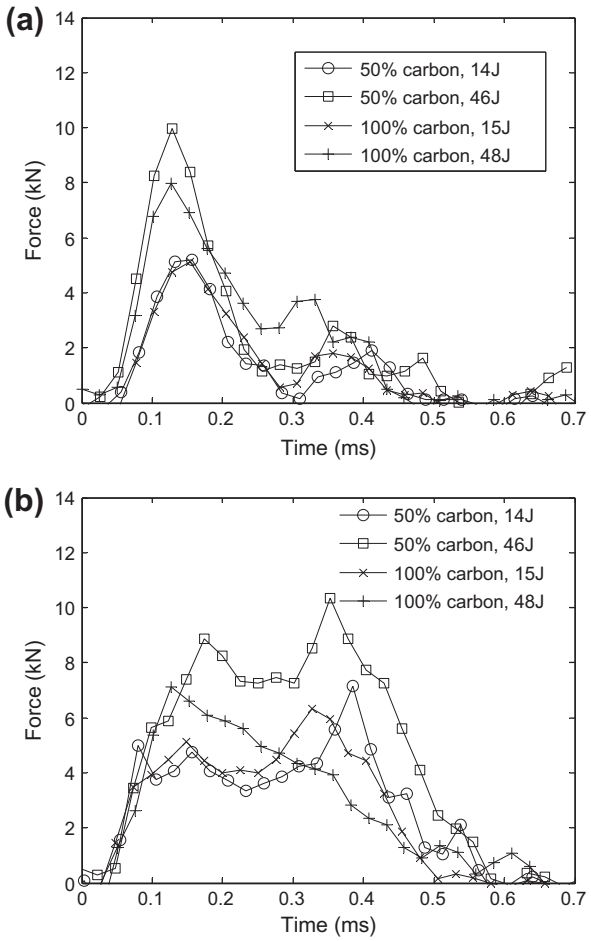

Fig. 15. Variation of contact force with time; (a) 12.5 g impactor and (b) 44.5 g impactor.

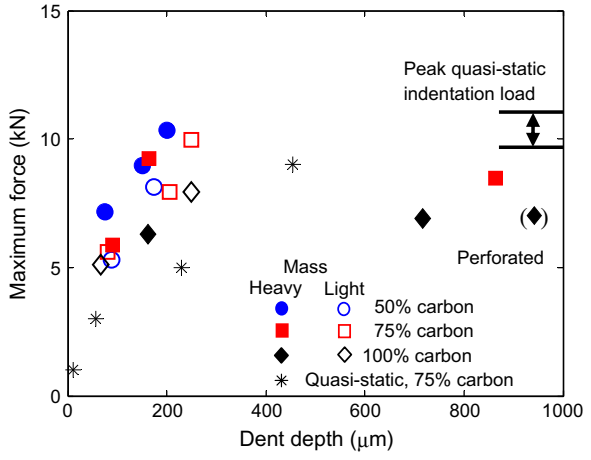

Fig. 16. Relationship between dent depth and maximum contact force.

dent depths measured for 75% carbon braid plates after quasi-static indentation. These quasi-static tests show significantly larger permanent indents, at the same force, compared with the general trend for the impacted specimens. Differences between the dent depth as a function of force for the quasi-static tests and the impacted samples may be due to differences in the local stresses, for example associated with plate inertia and changes in local bending strains, or due to strain rate sensitivity in the material. For the quasi-static indentation tests a peak was found in the indentation load, corresponding to severe fibre damage through the sample and effective penetration, in the range 9.75–11.5 kN for all three materials studied. This range of peak indentation loads is indicated in Fig. 16. The maximum contact force during impact never exceeds the peak indentation loads observed under quasi-static conditions, and indeed is considerably below this quasi-static limit for the three samples showing dent depths greater than 300 μm. At these higher contact loads, probably a more sophisticated analysis would be needed to understand how the plate bending response interacts with the local indentation field and how progressive fibre failure on the distal side and matrix failure on the impact side determine the perforation load.

Although the dent depth correlates reasonably well with the maximum force, there is a poor correlation between the maximum force and the C-scan area. This contrasts with the results of Cantwell [24], where a quasi-static model was found to capture the response.

9. Conclusions

This paper investigates the impact performance of 2D glass–carbon hybrid braided flat plates made using RTM which have been impacted using 12.5 and 44.5 g hemispherically-tipped projectiles at impact energies up to 50 J.

The effect of impact energy and speed on damage has been characterised for this class of material, with both quantitative measures of the damage and qualitative observations of damage mechanisms. Sectioning and X-ray images revealed significant amounts of matrix cracking leading to delamination and tow splitting, along with tow fibre breakage.

The effect of changes in the glass content of the braid has been characterised to help understand the trade-offs implicit in including glass in the hybrid braid weave. There is a 12% reduction in density changing from a 50:50 glass:carbon weave to a 100% carbon braid, while the axial stiffness E_1 of the composite increases by 36% and the effective plate bending stiffness under a central load increases by 29%. The amount of damage measured by C-scanning is significantly smaller for the 50% carbon braid, but similar for the 75% and 100% carbon braids. For the light impactor there is no apparent difference between materials in the depth of the permanent dent formed on the impact site, while for the heavy impactor the 100% carbon material has significantly deeper dents than the other materials at the same energy.

There are significant dynamic effects in these tests, which involved impact speeds up to 83 m/s. These affect both the inferred contact force history and the observed damage. These results highlight the importance of performing the impact experiments at speeds appropriate to service conditions and including plate response modes as well as the material local response in modelling the development of impact damage.

The compression-after-impact (CAI) strength of plates composed of 50% carbon material were measured. Impact damage was found to significantly reduce the strength, giving up to a 26% reduction at the maximum impact energy of around 45 J.

Acknowledgements

Contributions are gratefully acknowledged from the EPSRC (Grant EP/C538145/1), University of Nottingham, Cranfield University, Rolls-Royce plc., Dowty Propellers (Part of GE's Aviation Business), Carr Reinforcements Ltd., Laser Optical Engineering Ltd. and JR Technology Ltd. and colleagues at these organisations. The authors are grateful to Messrs Heaver, Thiruvenkatanathan and

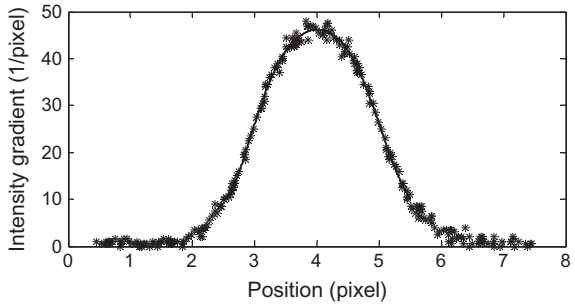

Fig. 17. Intensity gradient at the trailing edge of the impactor used to determine the position of the impactor. The data is a composite of 40 images, with each set of seven points centred on the estimated location of the peak in gradient. The smooth line through the data is a polynomial fit.

Mohagheghian, Dr. Lemanski and Prof. Woodhouse for technical assistance and advice.

Appendix A

This Appendix A provides additional justification for the accuracy of the acceleration measurements derived from high speed photography. As explained in Section 4.1, the location of the projectile is tracked by pinpointing the trailing edge. The location of the edge is first manually estimated from a contour plot of the intensity gradient function. A quadratic function is fitted through the three points around this maximum, and the position of the edge taken as the location of the maximum intensity gradient for this fitted function. It is hypothesised that errors in the determination of the edge arise from noise in the intensity gradient function at the edge. To determine the degree of noise in the signal, Fig. 17 plots the measured variation of the intensity gradient at the edge, combining together the data from 40 images corresponding to conditions of Fig. 4 (20 before contact and 20 during contact between the impactor and the plate). Each image contributes seven data points to this plot spaced a pixel apart, and the curve for each image has been centred on the estimated location of the maximum in the gradient, giving a random offset in pixel location between images and hence filling out the curve. Fig. 17 shows a remarkably consistent edge intensity gradient profile, reflecting the uniform lighting conditions and high quality camera. A polynomial function has been fitted to the data (shown as the solid line in Fig. 17) and the scatter in the gradient is estimated as the variation from this fit. It is clear that scatter is greater near the peak of the gradient function; the standard deviation in the intensity gradient is calculated as 1.26 intensity units/pixel for data within ±0.5 pixels of the peak, and 0.85 intensity units/pixel for data less than 2.5 pixels but more than 0.5 pixels from the peak. This is the relevant range for the edge detection algorithm.

Having established the experimental scatter in the gradient function, a stochastic simulation was undertaken to investigate the effect of this noise on the inferred acceleration. Sets of three data points representing intensity gradients at adjacent pixels were found from the smooth fitted gradient function, including random offsets from the peak. Then random noise in each of the data points was introduced, with the error being normally distributed with the standard deviations found in the previous paragraph. The location of the function maximum for this noisy data was then estimated using the quadratic fit algorithm described above, and the error between the peak estimated from this noisy data and the true peak location calculated. The standard deviation in the error in locating the peak in gradient from 1000 simulations spanning the range of possible pixel locations was found to be 0.029 pixels. This very high sub-pixel accuracy is possible because of the very reliable shape of the image edge, and is comparable to a sub-pixel accuracy of 0.02 pixels found in a similar first difference edge detection algorithm with a Gaussian spread in the edge intensity [25]. Finally a time series of edge locations was generated from this random error distribution. The procedure used to extract the acceleration of the impactor was applied to this series. Fig. 18 compares the inferred acceleration from a real test, Fig. 18a, with the acceleration given by the simulation containing just noise, Fig. 18b. Errors bands of ±0.015 m^2/s are included in both figures and seem to span the data for the real signal where the impactor is not contacting the plate, and for the acceleration generated from the noise. This confirms the hypothesis that the noise in the

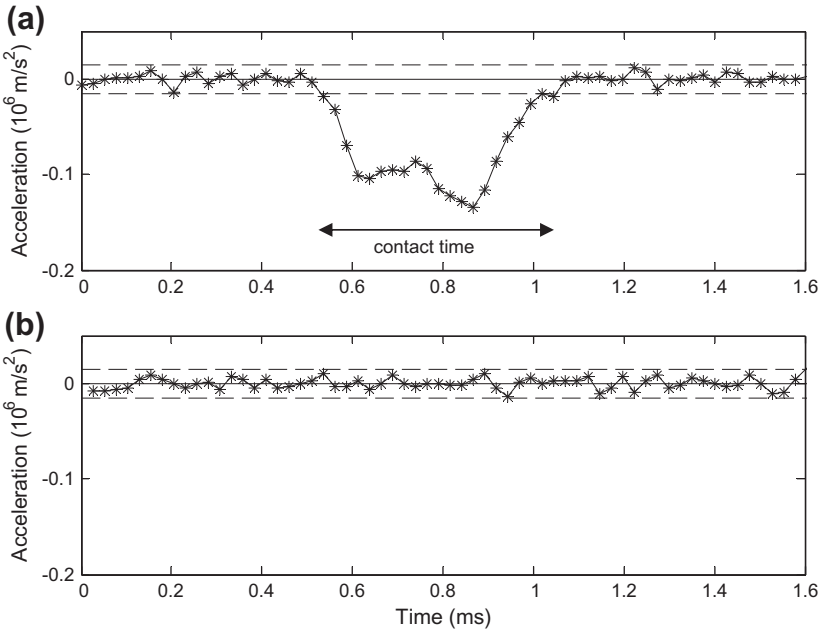

Fig. 18. Variation of acceleration with time: (a) experimental measurement, parameters as per Fig. 4 and (b) simulation of the inferred acceleration due only to noise in the intensity gradient measurement, using the spread of data given in Fig. 17. Graphs are to the same scale.

acceleration data is due to noise in the intensity images, and that the high accuracy of the inferred acceleration is attainable because of the very repeatable and clean intensity variation at the edge of the impactor.

References

[1] Tarim N, Findik F, Uzun H. Ballistic impact performance of composite structures. Compos Struct 2002;56:13–20.
[2] Griffiths B. Composite fan blade containment case. High Perform Compos 2005;13:76–8.
[3] Bibo GA, Hogg PJ. The role of reinforcement architecture on impact damage mechanisms and post-impact compression behaviour. J Mater Sci 1996;31:1115–37.
[4] Abrate S. Impact on composite structures. Cambridge University Press; 1998.
[5] Matemilola SA, Stronge WJ. Impact induced dynamic deformation and stresses in CFRP composite laminates. Compos Eng 1995;5:211–22.
[6] Curtis PT, Bishop SM. An assessment of the potential of woven carbon fibre-reinforced plastics for high performance applications. Composites 1984;15(4):259–65.
[7] Hosur MV, Islam MM, Jeelani S. Low-velocity impact response of braided carbon/epoxy composites. in: ICCES 6(1) 81–89, Proceedings of the international conference of computational and experimental engineering and sciences, ICCES '08, Honolulu, HI; March 15–21, 2008.
[8] Saka K, Harding J. A simple laminate theory approach to the prediction of the tensile impact strength of woven hybrid composites. Composites 1990;21(5):439–47.
[9] Sayer M, Bektaş NB, Sayman O. An experimental investigation on the impact behavior of hybrid composite plates. Compos Struct 2010;92:1256–62.
[10] Hosur MV, Abdullah M, Jeelani S. Studies on the low-velocity impact response of woven hybrid composites. Compos Struct 2005;67:253–62.
[11] Sevkat E, Liaw B, Delale F, Raju BB. Drop-weight impact of plain-woven hybrid glass-graphite/toughened epoxy composites. Composites: Part A 2009;40:1090–110.
[12] Enfedaque A, Molina-Aldareguía JM, Gálvez F, González C, Llorca J. Effect of glass fiber hybridization on the behavior under impact of woven carbon fiber/epoxy laminates. J Compos Mater 2010;44:3051–68.
[13] von Reden T, Bulat M, Dreshsler K. Mechanical performance of hybrid carbon glass fibre braids with a high ratio of 0°-fibres. In: Binetry C, Boussu F, editors. Recent advances in textile composites (proceedings of Texcomp 10) ed. Destech Publications Inc.; 2010. p. 514–20.
[14] Bahei-El-Din YA, Zikry MA. Impact-induced deformation fields in 2D and 3D woven composites. Compos Sci Technol 2003;63(7):923–42.
[15] Ollson R. Mass criterion for wave controlled impact response of composite plates. Composites: Part A 2000;31:879–87.
[16] Corum JM, Battiste RL, Ruggles-Wrenn MB. Low-energy impact effects on candidate automotive structural composites. Compos Sci Technol 2003;63:755–69.
[17] Matemilola SA, Stronge WJ. Rate effect for impact damage initiation in CFRP laminates. Journal de Physique IV, Colloque C8 1994;4:225–30.
[18] Zumpano G, Fox M, Stronge WJ, Sutcliffe MPF. Impact damage in hybrid braided twill composites. J Mater Sci 2008;43(20):6668–75.
[19] McIntyre ME, Woodhouse J. On measuring the elastic and damping constants of orthotropic sheet materials. Acta Metall 1988;36:1397–416.
[20] McMillan AJ, Monroy Aceves C, Sutcliffe MPF. Moderate energy impact analysis combining phenomenological contact law with localised damage and integral equation method. Int J Impact Eng 2012;43:29–39.
[21] Lobo L, Tyler JR. Residual lifetime prediction of bonded composites structures using in-plane laser shearography. In: SAMPE Conference. Composites – Innovative materials for smarter solutions, Paris; 23–25th March; 2009.
[22] Polimeno U, Meo M, Almond DP, Anfioni SL. Detecting low velocity impact damage in composite plate using nonlinear acoustic/ultrasound methods. Appl Compos Mater 2010;17:481–8.
[23] Moffat AJ, Wright P, Helfen L, Baumbach T, Johnson G, Spearing SM, et al. In-situ synchrotron computed laminography of damage in carbon fibre–epoxy $[09/0]_s$ laminates. Scr Mater 2010;62:97–100.
[24] Cantwell WJ. Geometrical effects in the low velocity impact response of GFRP. Compos Sci Technol 2007;76:1900–8.
[25] Overington I, Greenway P. Practical first-difference edge detection with subpixel accuracy. Image Vision Comput 1987;5:217–24.